Journal of the Optical Society of America B
OPTICAL PHYSICS

Tunable hyperbolic photonic devices based on periodic structures of graphene and HfO_2

Susobhan Das, Alessandro Salandrino, and Rongqing Hui

Department of Electrical Engineering and Computer Science, The University of Kansas, Lawrence, Kansas 66045, USA
**Corresponding author: rhui@ku.edu*

Received 31 May 2018; revised 3 August 2018; accepted 28 August 2018; posted 29 August 2018 (Doc. ID 332977); published 26 September 2018

One of the unique characteristics of hyperbolic metamaterials (MMs) is the possibility of accessing various regimes of extreme anisotropy. Here, we propose a MM based on periodic layers of hafnium oxide (HfO_2) and monolayer graphene. Based on the fact that graphene permittivity can be controlled by changing its chemical potential via externally applied electric voltage, we theoretically investigate the anisotropic behavior of the proposed MM as the function of the external electrical bias. Based on our findings, we provide examples of possible nanophotonic device applications based on such tunable hyperbolic MMs. Prototypes of a polarizer, a modulator, and a MM-assisted tunable coupler are investigated at the 1550 nm communication wavelength. Additionally, we show that the high tuning efficiency of MMs allows a miniaturized device to be realized with enhanced functionality per area for photonic integration.

OCIS codes: (160.3918) Metamaterials; (250.5403) Plasmonics; (130.4110) Modulators.

https://doi.org/10.1364/JOSAB.35.002616

1. INTRODUCTION

The advent of metamaterials (MMs) in the past two decades has led to a variety of new possibilities for the control of electromagnetics, with a potentially transformative impact in the design of integrated photonic circuits. Squeezing, tunneling, and confining below the light diffraction limit are some of the effects enabled by optical MMs [1–3]. Various novel structures based on plasmonic effects have been proposed and investigated over the past decade to redesign optical components, such as filters, modulators, and sensors, with high tuning efficiency and considerably miniaturized device size [4–9]. As an example, epsilon-near-zero (ENZ) MMs have been exploited to produce strong field enhancement over small spatial regions, which in turn can be exploited to enhance the interaction between optical field and the material in these regions. By utilizing the extraordinary properties of electromagnetic propagation in ENZ material for the design of photonic devices can increase the bandwidth of operation, decrease the power consumption, and increase the functionality per area (FPA) [10,11], which is a basic figure of merit for integrated photonic devices. The rapid advancement of nanotechnology also enabled the creation of various types of MMs, which led to a variety of novel ideas and applications such as cloaking and sub-diffraction imaging [12–17].

To exploit MM properties in active optoelectronic applications such as modulation and switching, it is necessary to have a tuning mechanism for the electromagnetic properties of the structures and/or the constituent materials. Graphene, which has been investigated extensively over the past decade, appears to be an excellent candidate for providing such tunability. The complex refractive index of graphene is a function of its chemical potential, which can be controlled by external electrical biasing [18]. The combination of graphene and a MM in plasmonic structures can provide unprecedented functionality and tunability for integrated photonic circuits. More specifically, a MM composed of periodic graphene and dielectric layers can create a highly efficient tunable hyperbolic medium, ideal for electro-optic device applications [19]. In not only the NIR region, but also in the terahertz region, layered graphene structures have shown excellent performance in the form of different devices, such as quarter-wave plates [20] and amplifiers [21].

In this work, we propose an active MM composed of periodic layers of hafnium oxide (HfO_2) and a single layer of graphene, and theoretically analyze its basic properties. Because of the tunability of graphene permittivity through the change of its chemical potential, the proposed MM offers electronic control of its anisotropic optical properties. As application examples of this MM, we provide structural design and performance assessment of several functional devices, including polarizers, electro-optic modulators, and directional couplers, for operation at the 1550 nm optical communication wavelength. While conventional polarizers and directional couplers have fixed values of extinction ratio and coupling coefficient upon which the devices are made, the proposed polarizers and couplers are electrically tunable. In comparison to existing silicon photonic electro-absorption (EA) modulators based on a single layer or two layers of graphene [22,23], the electro-optic

modulation efficiency of the proposed modulator is much higher, depending on the layers of graphene used, and thus the device footprint can be greatly reduced.

2. DESIGN AND OPTICAL PROPERTIES OF MM

The unit cell of the MM proposed here is formed by two different materials of permittivities ε_1 and ε_2 with thickness d_1 and d_2, respectively. The periodicity is thus denoted by $d_T = d_1 + d_2$. For mathematical simplicity, individual layer thickness is represented by the fractions of d, i.e., $d_1 = c_1 d_T$ and $d_2 = c_2 d_T$, where c_1 and c_2 are dimensionless, satisfying $c_1 + c_1 = 1$. This type of artificial material is inherently anisotropic. Additionally, the selection of materials with permittivities of ε_1 and ε_2 and coefficients c_1 and c_2 provide the degrees of freedom required for the design of complex media for various applications. The periodicity d of the layered MM must be much smaller than the operating wavelength, such that the incident EM waves should see it effectively as a homogeneous medium rather than a multilayer material. Considering the periodicity along the y axis (perpendicular to the graphene plane) indicated in Fig. 1(a), the permittivity tensor of the anisotropic MM can be represented as

$$\bar{\varepsilon} = \varepsilon_0 \begin{bmatrix} \varepsilon_T & 0 & 0 \\ 0 & \varepsilon_L & 0 \\ 0 & 0 & \varepsilon_T \end{bmatrix},$$
$$\text{with} \quad \varepsilon_T = c_1\varepsilon_1 + c_2\varepsilon_2 \quad \text{and} \quad \varepsilon_L = \frac{\varepsilon_1\varepsilon_2}{c_1\varepsilon_2 + c_2\varepsilon_1}, \tag{1}$$

where ε_T and ε_L represent the transvers and longitudinal permittivities, respectively, of the anisotropic MM. This structure has been extensively studied by several groups for different purposes, with an emphasis on the hyperbolic dispersion properties arising when $\text{Sign}(\varepsilon_L) \neq \text{Sign}(\varepsilon_T)$ [12–15].

Considering the feasibility of the proposed structure, a HfO_2 layer and a monolayer graphene have been chosen to frame the unit cell of the MM. The schematic of the MM is shown in Fig. 1(a). Graphene layers are interleaved for connection to the opposite sides of an electrode, which allows electrical biasing to change the chemical potential μ_c. The standard mathematical model of HfO_2 permittivity ε_{HfO_2} in the 1550 nm wavelength window is used [24]. The well-known Kubo formula [18] is used to represent the single layer graphene conductivity:

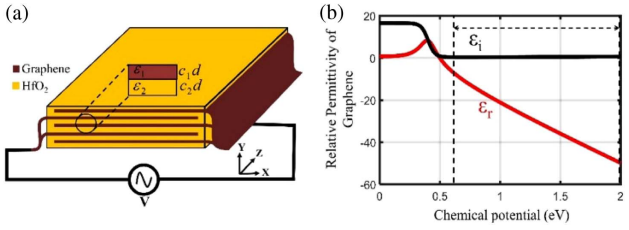

Fig. 1. (a) Schematic diagram of a MM that consists of periodic layer of HfO_2 and monolayer graphene. (b) Real (ε_r) and imaginary (ε_i) parts of single-layer graphene permittivity $\varepsilon_{GR}^{\parallel}$ at 1550 nm wavelength as a function of chemical potential.

$$\sigma(\omega, \mu_c, \Gamma, T) = \frac{je^2(\omega - 2j\Gamma)}{\pi\hbar^2} \times \left\{ \frac{1}{(\omega - j2\Gamma)^2} \int_0^\infty \varepsilon \left[\frac{\partial f_d(\varepsilon)}{\partial\varepsilon} - \frac{\partial f_d(-\varepsilon)}{\partial\varepsilon} \right] d\varepsilon - \int_0^\infty \frac{f_d(\varepsilon) - f_d(-\varepsilon)}{(\omega - j2\Gamma)^2 - 4(\varepsilon/\hbar)^2} d\varepsilon \right\}, \tag{2}$$

which is the combination of the inter-band and intra-band absorptions represented by the first and the second terms, respectively. ω is the optical frequency, e is the electron charge, $\hbar = h/2\pi$ is the reduced Planck constant, and $f_d = 1/(e^{(\varepsilon-\mu_c)/k_BT} + 1)$ is the Fermi–Dirac distribution function. ε is the energy, k_B is Boltzmann's constant, $T = 300$ K is the absolute temperature, $\Gamma = 5$ meV is the scattering parameter, and μ_c is the chemical potential. The conductivity predicted by Eq. (2) can be converted into an in-plane complex permittivity based on $\varepsilon_{GR}^{\parallel} = 1 - j\sigma/(\omega\varepsilon_0\delta_g)$, where ε_0 is the free space permittivity, and $\delta_g = 0.34$ nm is the thickness of monolayer graphene. It is worth noting that the permittivity perpendicular to the graphene plane, $\varepsilon_{GR}^{\perp}$, is unity. $\varepsilon_{GR}^{\parallel}$ can be tuned by charge doping or chemical potential change through externally applied voltage. The real and the imaginary parts of $\varepsilon_{GR}^{\parallel}$ at 1550 nm wavelength as the function of its chemical potential are shown in Fig. 1(b). This provides the mechanism of tuning ε_T of the proposed MM electronically. It is evident from Fig. 1(b) that within the chemical potential range from 0.57 to 2 eV, as marked by two vertical dashed lines, the imaginary part of $\varepsilon_{GR}^{\parallel}$ is nearly zero and remains almost invariant, while the real part of $\varepsilon_{GR}^{\parallel}$ becomes more negative with the increase of chemical potential.

To achieve such a high level of chemical potential, a high electric field is needed that requires the dielectric material to have high electrical breakdown field, E_{bd}. Normally, bulk HfO_2 has an E_{bd} of lower than 1 MV/cm. However, when its thickness goes down to nanometer scale, E_{bd} becomes significantly higher and attains a breakdown electric field as high as $E_{bd} \approx 60$ MV/cm [25]. The breakdown of nanometer-thick HfO_2 film is most likely initiated by bond rupturing rather than point defects, as happens in bulk HfO_2 [25].

In our modeling of a MM, the design parameters are taken as $d_T = 3$ nm for the periodicity, $d_1 = 0.34$ nm for the thickness of the monolayer graphene, and $d_2 = 2.66$ nm for the HfO_2 film. Following the permittivity tensor of Eq. (1) for anisotropic MM, ε_T and can be represented as

$$\varepsilon_T = c_1\varepsilon_{GR}^{\parallel} + c_2\varepsilon_{HfO_2} \quad \text{and} \quad \varepsilon_L = \frac{\varepsilon_{GR}^{\perp} + \varepsilon_{HfO_2}}{c_1\varepsilon_{HfO_2} + c_2\varepsilon_{GR}^{\perp}}, \tag{3}$$

where $c_1 = 0.11333$, $c_2 = 0.88667$, $\varepsilon_{GR}^{\perp} = 1$. $\varepsilon_{GR}^{\parallel}$ and ε_{HfO_2} can be obtained from a standard formula as mentioned previously [18,19]. It is clear from Eq. (2) that only ε_T is tunable as a function of chemical potential through $\varepsilon_{GR}^{\parallel}$. Considering the design parameters and the thickness of HfO_2 layer, an external voltage tuning from 1.1 to 13.75 V is required to change the chemical potential of graphene from 0.57 to 2 eV. This was obtained from the oxide capacitance calculation [18], with $\mu_c = \hbar v_F \sqrt{\pi\varepsilon_{HfO_2}(V - V_D)/ed_2}$,

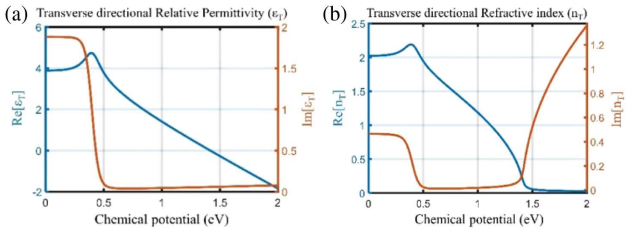

Fig. 2. Real and imaginary parts of transverse directional (a) permittivity and (b) refractive index of MM at 1550 nm wavelength as a function of chemical potential.

where $v_F = 0.75 \times 10^6$ m/s is the Fermi velocity, V_D is the Dirac voltage determined by the initial doping of the graphene, and V is the externally applied voltage.

Within this voltage range, the maximum electric field strength inside the dielectric HfO_2 layer will be 51.7 MV/cm, which is still less than the breakdown field of nanometer-thick HfO_2 [24]. Since the permittivity perpendicular to the graphene plane is $\varepsilon_{GR}^{\perp} = 1$, the longitudinal permittivity of the MM, $\varepsilon_L = 3.13$, will be a pure dielectric that does not change with the graphene chemical potential. The transversal permittivity and the refractive index of the proposed MM at 1550 nm wavelength as a function of graphene chemical potential is shown in Fig. 2. Both the permittivity and the refractive index of the proposed MM change drastically over the chemical potential range from 0 to 2 eV. The real part of ε_T becomes zero around 1.4 eV and, therefore, this MM can be treated as ENZ material around this chemical potential level. Above 1.4 eV of chemical potential, transversal permittivity of this MM becomes negative, where MM can be implemented as a hyperbolic material.

In the lower chemical potential range from 0 to 0.8 eV, although the real part of transversal permittivity remains positive, there is a drastic change in the imaginary part, which represents the change of material loss for an optical signal polarized along the transversal direction. Therefore, based on specific application and desired functionality, we can select the proper range of chemical potential to design photonic devices in which a MM offers the maximum performance and tuning efficiency. We can also dope the graphene with a chemical potential at the middle of the operation region, and thus reduce the maximum externally applied voltage to avoid electric breakdown in the HfO_2 layers.

3. APPLICATIONS

Based on the optical properties of the proposed MM shown in Fig. 2(a), it can be utilized to implement various photonic devices in an integrated photonic circuit platform. In this section, we describe a few possible photonic devices, including polarizers, modulators, and tunable directional couplers, that can be made with the proposed MM. The expected performance of these devices is provided through modeling and numerical simulations.

A. Polarizer

The basic working principle of an optical polarizer is to pass or block the optical signal of a specific state of polarization [26].

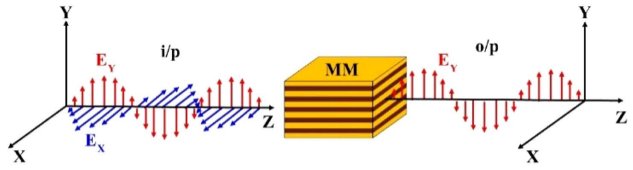

Fig. 3. Schematic diagram of a polarizer based on a MM.

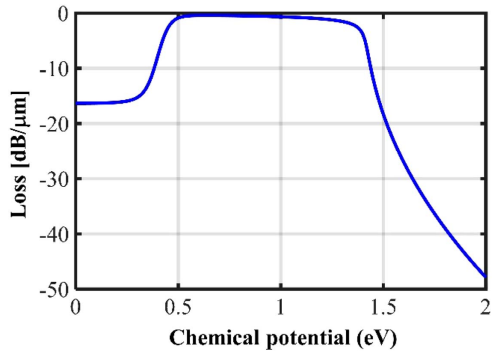

Fig. 4. Propagation loss of x-polarized light through a MM at 1550 nm wavelength.

The schematic diagram of the polarizer based on the proposed MM is shown in Fig. 3. The orientation of the MM is in such a way that the layers of HfO_2 and monolayer graphene are stacked along the y direction, and the propagation direction of the EM wave is along the positive z direction, as shown in Fig. 3.

In this particular orientation, x-polarized and y-polarized EM waves see the MM as an isotropic medium with permittivities ε_T and ε_L, respectively. Since longitudinal relative permittivity ε_L of the MM is a real number that is independent of the graphene chemical potential, there is no path loss for an optical signal polarized in the y direction when propagating through the MM. On the other hand, the transversal permittivity ε_T of the MM is complex, and is a function of graphene chemical potential, as shown in Fig. 2, and, thus, an x-polarized optical signal will suffer from a loss when propagating through the MM. The path loss of an x-polarized EM wave as a function of graphene chemical potential is shown in Fig. 4. Since ideally there is no path loss for y-polarized EM waves, Fig. 4 also represents the extinction ratio of the polarizer.

Noticeably, within the range of chemical potential from 0.5 to 1.4 eV, the extinction ratio is very low and the MM is essentially not polarization selective in this region. Apart from this range, the extinction ratio of the polarizer is largely tunable and can reach as high as 48 dB/μm at 2 eV of chemical potential. Without applying the bias voltage, the extinction is of the order of 16 dB/μm, which corresponds to an approximately 97% degree of polarization (DoP).

B. Modulator

An electro-optic modulator is one of the basic components to encode an electronic signal onto an optical carrier [7,10,11]. The schematic diagram of a modulator based on the proposed MM is shown in Fig. 5(a). The proposed MM is embedded at

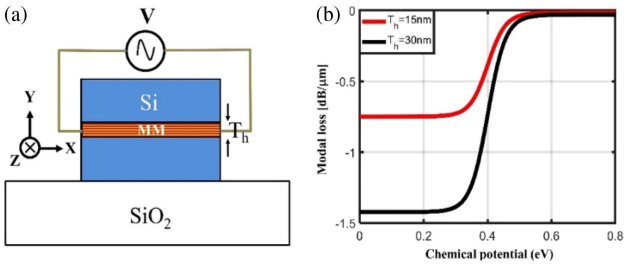

Fig. 5. (a) Schematic diagram of MM-assisted modulator and (b) modal loss for x-polarized guided fundamental mode over chemical potential for two different thicknesses of MM (15 and 30 nm) at 1550 nm wavelength.

the middle of the silicon ridge waveguide of cross section 420 nm × 300 nm, which can be fabricated on a silicon-on-insulator (SOI) wafer. As the fundamental mode guided by the waveguide has the maximum field intensity at the central position of the waveguide, imbedding the MM in the middle of the waveguide allows the strongest interaction between the guided mode and the MM.

As the embedded MM layers are parallel to the x–z plane, the x-polarized fundamental mode can be modulated by changing the chemical potential of graphene. Additionally, increasing the MM thickness at the middle of the waveguide will increase the interaction between the modal field and the MM. The propagation loss of the x-polarized fundamental mode is calculated for two different MM layer thicknesses, and the results are shown in Fig. 5(b). For each thickness, the maximum and the minimum modal loss are found at 0 and 0.8 eV chemical potential, respectively. Therefore, binary electro-optic modulation can be accomplished by switching the chemical potential between 0 and 0.8 eV by changing external application of voltage 0 and 2 V, respectively, to achieve optical modulation depths of 0.73 dB/μm for 15 nm MM thickness and 1.4 dB/μm for 30 nm MM thickness. This is about 1 order of magnitude higher than silicon photonic modulators based on a single layer or two layers of graphene [27,28]. For a 13 dB modulation depth usually required in fiber-optic communications, device lengths of 10 and 18 μm will be needed. The modulation speed of the modulator depends mainly on the capacitance formed by each pair of graphene layers that form the MM. Based on a straightforward estimation, the capacitance of the 30 nm MM is approximately 0.3 pF/μm. For a 10 μm modulator length to achieve 13 dB modulation depth, and assuming a 50 Ω matched load impedance, the modulation bandwidth is about 2.5 GHz. This is comparable to the 1 GHz bandwidth of the similar graphene-based EA modulators reported in [22,23], except where the modulator length is much longer but the capacitance per unit length is smaller.

C. Directional Coupler

Directional coupler is one of the most important basic building blocks to construct a photonic circuit. When two waveguides are placed in close proximity, optical power from one waveguide can be transferred to the other waveguide and vice versa via evanescent field coupling. The coupling coefficient depends not only on the separation between the two waveguides, but it also depends on the optical properties of the material in the coupling region that separates the two waveguides. Conventionally, the dielectric material in the coupling region is homogeneous, such as silica or air. Here, we propose to insert the tunable anisotropic MM discussed above as the dielectric spacer between the two waveguides in the coupling region. This will allow dynamic tuning of the coupling coefficient.

The basic cross-section structure in the coupling region of a photonic coupler is shown in Fig. 6(a), in which two planar waveguides (WG_1 and WG_2) are separated by an anisotropic medium. Although numerical simulation can be used to calculate the coupling coefficient, theoretical formulation and analysis are important to understand the basic physical mechanisms and design rules. To simplify the analysis, the guided fundamental modes are first studied in the structure shown in Fig. 6(b), in which one side of the waveguide is the anisotropic medium and other side is air.

In this analysis we assume $\varepsilon_{\text{air}} < \varepsilon_{\text{am}} < \varepsilon_{\text{WG}}$, where ε_{air}, ε_{am}, and ε_{WG} are the permittivities of air, the anisotropic medium, and the waveguide, respectively. The planar structure is infinitely extended along the y direction and the guided mode is propagating along the z direction. For the sake of simplicity, orientation of the anisotropic material is chosen in such a way that it holds the relation $\varepsilon_x = \varepsilon_z \neq \varepsilon_y$, where ε represents the permittivity along the direction indicated by the subscript. Thus, the relation between the electric field $\vec{E}$ and the electric flux density tensor $\vec{D}$ can be expressed as

$$\vec{D} = \varepsilon_0 \begin{bmatrix} \varepsilon_x & 0 & 0 \\ 0 & \varepsilon_y & 0 \\ 0 & 0 & \varepsilon_x \end{bmatrix}. \tag{4}$$

Considering the electric field orientation, the guided fundamental modes of the planar waveguide can be classified into TE mode and TM mode [29].

The TE mode has field components H_x, E_y, and H_z, and, based on Maxwell's equations, their relationship can be written as

$$j\beta_{\text{TE}} E_y = -j\omega\mu_0 H_x, \tag{5a}$$

$$\frac{\partial E_y}{\partial x} = -j\omega\mu_0 H_z, \tag{5b}$$

$$j\beta_{\text{TE}} H_x + \frac{\partial H_z}{\partial x} = -j\omega\varepsilon E_y, \tag{5c}$$

where β_{TE} is the propagation constant of the guided TE mode. For the air and the waveguide medium with permittivities ε_0 and ε_{WG}, respectively, the wave equations are isotropic in both regions. In the anisotropic medium, because the electric field

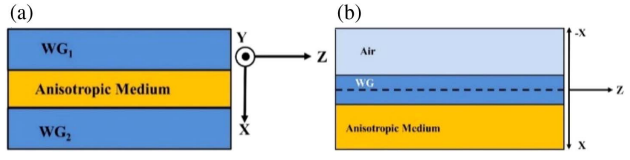

Fig. 6. Schematic diagram of (a) planar-waveguide-based coupler with an anisotropic medium as a dielectric spacer and (b) the single planar waveguide with an anisotropic medium on one side.

has only the E_y component, the medium is equivalently isotropic with a permittivity ε_y. Therefore, for the TE mode, the wave equation can be simplified as

$$\frac{\partial^2 E_y}{\partial x^2} + (\omega^2 \mu_0 \varepsilon - \beta_{\mathrm{TE}}^2) E_y, \tag{6}$$

where ε represents ε_0, $\varepsilon_{\mathrm{WG}}$, and ε_y for air, the waveguide, and the anisotropic medium, respectively.

Similarly, for the TM mode with E_x, H_y, and, E_z, Maxwell's equations relating these field components are

$$j\beta_{\mathrm{TM}} E_x + \frac{\partial E_z}{\partial x} = -j\omega\mu_0 H_y, \tag{7a}$$

$$j\beta_{\mathrm{TM}} H_y = -j\omega\varepsilon E_x, \tag{7b}$$

$$\frac{\partial H_y}{\partial x} = -j\omega\varepsilon E_z, \tag{7c}$$

where β_{TM} is the propagation constant of the guided TM mode. Since the electric field has both E_x and E_z components, the permittivity along the x and the z directions have to be used in the TM mode field equations. However, considering the orientation of the anisotropic material, permittivities along the x and z directions are equal, and thus ε can be replaced by ε_x in the anisotropic medium in this case. Therefore, the wave equation for the TM mode is

$$\frac{\partial^2 H_y}{\partial x^2} + (\omega^2 \mu_0 \varepsilon - \beta_{\mathrm{TM}}^2) H_y, \tag{8}$$

where ε represents ε_0, $\varepsilon_{\mathrm{WG}}$, and ε_x for air, the waveguide, and the anisotropic medium, respectively.

This analysis indicates that TE and TM modes in a planar waveguide sandwiched between air and an anisotropic medium can be analyzed independently, and the anisotropic medium can be simplified to a homogeneous medium with permittivity ε_y and ε_x, respectively, for these two modes.

Now, considering the actual waveguide coupler's cross section, Fig. 7 shows the permittivity distribution along the x direction, where $\varepsilon_{\mathrm{am}}$ is the permittivity of the anisotropic MM. The width of the waveguide is $2a$ with $2d$ separation at the coupling region, as shown in Fig. 7.

By applying the coupled-mode theory on a rectangular waveguide directional coupler [30], the coupling coefficients for TE and TM can be expressed as

$$k_{\mathrm{TE}} = \frac{h^2 p_{\mathrm{am}} e^{-2p_{\mathrm{am}}d}}{\beta a (h^2 + p_{\mathrm{am}}^2)\left(1 + \frac{1}{2p_0 a} + \frac{1}{2p_{\mathrm{am}} a}\right)},$$

$$k_{\mathrm{TM}} = \frac{\frac{\varepsilon_{\mathrm{WG}}}{\varepsilon_{\mathrm{am}}} h^2 p_{\mathrm{am}} e^{-2p_{\mathrm{am}}d}}{\beta a\left(h^2 + \frac{\varepsilon_{\mathrm{WG}}}{\varepsilon_{\mathrm{am}}} p_{\mathrm{am}}^2\right)} \times \left(1 + \frac{1}{2p_0 a}\frac{\varepsilon_{\mathrm{WG}}}{\varepsilon_0}\frac{h^2 + p_0^2}{h^2 + \frac{\varepsilon_{\mathrm{WG}}}{\varepsilon_0} p_0^2} + \frac{1}{2p_{\mathrm{am}} a}\frac{\varepsilon_{\mathrm{WG}}}{\varepsilon_{\mathrm{am}}}\frac{h^2 + p_{\mathrm{am}}^2}{h^2 + \frac{\varepsilon_{\mathrm{WG}}}{\varepsilon_{\mathrm{am}}} p_{\mathrm{am}}^2}\right)^{-1}, \tag{9}$$

where the field variation in the x direction is $\cos(hx)$ inside the waveguide, with β as the propagation constant. p_0 and p_{am} are the exponential decay coefficients in the region of permittivities ε_0 and $\varepsilon_{\mathrm{am}}$, respectively.

As the coupling coefficient is very sensitive to material permittivity and its distribution in the coupling region, using anisotropic material as the dielectric spacer allows the construction of a mode-dependent coupler. However, based on a conventional anisotropic dielectric material, the anisotropy of the material cannot be dynamically modified. The electrically controllable permittivity tensor of the MM proposed here provides an enabling mechanism for tuning.

Two different configurations of 3D directional couplers based on the tunable MM are shown in Fig. 8. To manipulate the coupling of the x-polarized EM wave of the guided fundamental mode, the layers of MM are oriented parallel to the x–z plane, whereas for y-polarization, the MM orientation will be along the y–z plane, as shown in Figs. 8(a) and 8(b), respectively. Because of the evanescent field coupling between two waveguides, the coupling coefficient can be modeled using Eq. (12).

By varying the Re[$\varepsilon_{\mathrm{am}}$] from 0.067 to 3.8, the coupling coefficient obtained from Eq. (12) for both the TE and TM modes is shown in Fig. 9.

It is very prominent from Fig. 9 that the variation of coupling coefficient with change of the permittivity of the dielectric spacer has stronger impact for the TM mode compared to the TE mode.

The top view schematic diagram of the proposed MM-assisted photonic coupler (hyper-coupler) is shown in Fig. 10. It can be fabricated based on silicon ridge waveguides on a SOI wafer. The two waveguides (as denoted by WG_1 and WG_2) have identical cross sections of 420 nm × 300 nm, and they are far apart from each other except for the coupling region. The space between the two waveguides within the coupling region is filled with the anisotropic MM. To characterize the proposed MM-assisted coupler, the COMSOL Multiphysics software package is used, which is a numerical solver based on the 2D finite-element method (FEM).

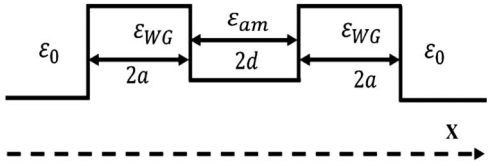

Fig. 7. Space-dependent permittivity distribution of coupled waveguides with an anisotropic MM as a dielectric spacer.

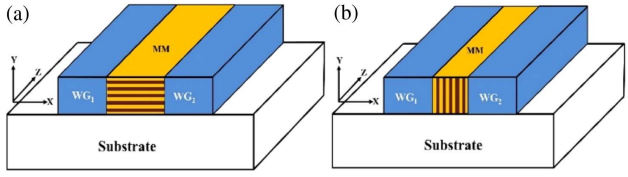

Fig. 8. 3D Schematic diagram of a directional coupler for (a) x-polarized and (b) y-polarized guided fundamental modes.

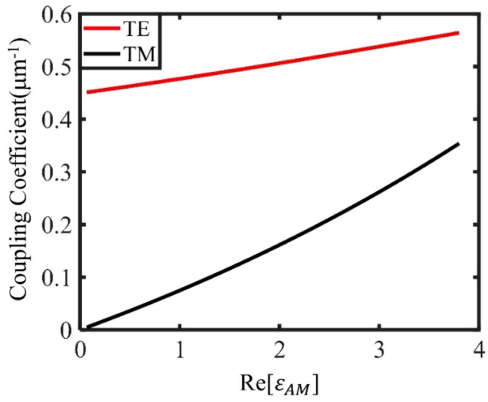

Fig. 9. Coupling coefficient calculation based on Eq. (12) for both TE and TM modes with an anisotropic MM as dielectric spacer.

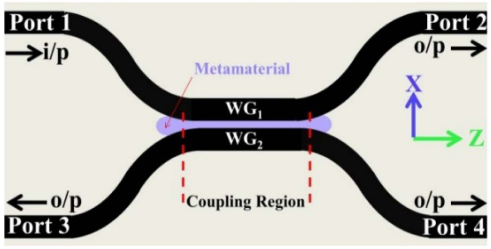

Fig. 10. Schematic diagram of MM-assisted photonic coupler based on silicon ridge waveguides.

For the x-polarized guided fundamental mode, the length of the coupling region is 5 μm, and the separation between the two waveguides is 90 nm. The anisotropic MM in the coupling region is oriented in such a way that $\varepsilon_x = \varepsilon_z = \varepsilon_T$ and $\varepsilon_y = \varepsilon_L$. In the simulation, an x-polarized fundamental mode at 1550 nm wavelength is launched into port 1 of the coupler illustrated in Fig. 8(a). For the application as a directional coupler, the output power from port 3 is ideally zero, and the total output power will split between port 2 and port 4.

In the absence of MM and considering air as the medium in the coupling region between the two waveguides, the x-polarized fundamental mode coupling coefficient at 1550 nm wavelength is approximately 0.0926/μm, corresponding to a coupling length of approximately 17 μm. Figure 11(a) shows that, after incorporating the MM into the gap between the two waveguides in the coupling region, the coupling coefficient is enhanced by more than threefold at 0.57 eV chemical potential, which reduces the length of the coupling region by the same factor. The power outputs from port 2 (P_2) and port 4 (P_4) for the MM-assisted coupler are shown in Fig. 11(b), and are normalized by the input power from port 1 (P_{in}). It is prominent from Fig. 11 that, within the chemical potential range from 0.57 to 1.32 eV, the coupling coefficient reduces monotonically, and the optical signal completely switches from port 4 to port 2. Because of the index discontinuity at the interface between the MM and the surrounding air in the coupling region, optical scattering was introduced, which created approximately 10% insertion loss within the range of concern of graphene's chemical potential.

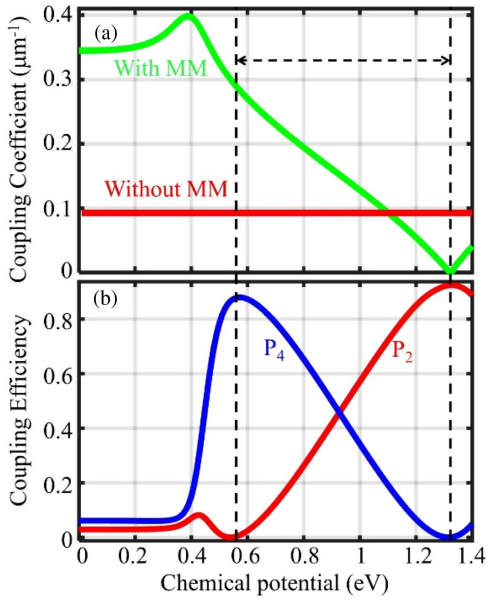

Fig. 11. (a) Coupling coefficient of the coupler with and without MM in the coupling region. (b) Normalized power output from port 2 and port 4 in terms of coupling efficiency as a function of chemical potential.

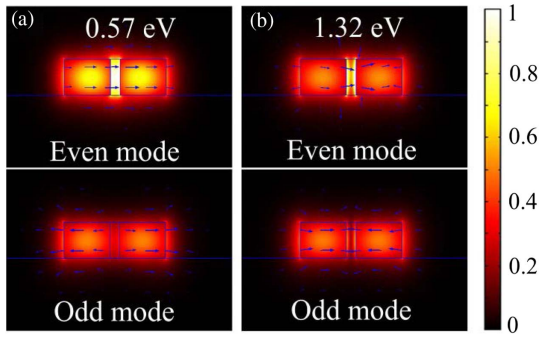

Fig. 12. Normalized even and odd modal electric fields with polarization indicated by arrow streams at chemical potential of (a) 0.57 eV and (b) 1.32 eV.

Thus, the maximum normalized coupling efficiency is slightly less than unity. Below 0.57 eV of chemical potential, even though the coupling coefficient shown in Fig. 11(a) is high, the coupling efficiency is very low because the MM is highly absorptive in this region. The normalized modal fields of even and odd modes at the cross section of the coupling region are shown in Figs. 12(a) and 12(b), corresponding to chemical potential of 0.57 and 1.32 eV, respectively. The arrow stream indicates the field polarization of the modes.

Normalized electric field profiles of beam propagation through the directional coupler biased at 0.57 and 1.32 eV chemical potential are shown in Figs. 13(a) and 13(b), respectively. At 0.57 eV chemical potential, more than 90% of the power from WG_1 is coupled to WG_2 because of the high coupling coefficient. However, at 1.32 eV chemical potential, the coupling coefficient is very low so that most of the power remains confined in WG_1 and emerges from output port 2.

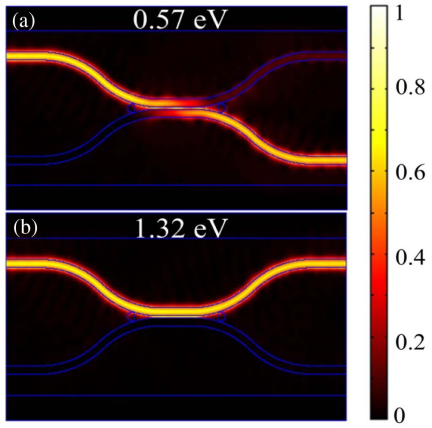

Fig. 13. Normalized electric field plot at chemical potential of (a) 0.57 eV and (b) 1.32 eV.

Within the range of chemical potential between 0.57 and 1.32 eV, the monotonic change in coupling efficiency offers the capability of not only digital switching but also analog modulation of the output power between the two output ports through the modulation of the chemical potential, equivalent to a range of biasing voltage between 1.1 and 6 V in this example.

Similarly, consider the y-polarized fundamental mode of 1550 nm wavelength launched into port 1 of the coupler shown in Fig. 10(b). Simulation results show that the length is 2.8 μm when the separation between the two waveguides is 60 nm. The anisotropic MM in the coupling region is oriented in such a way that $\varepsilon_y = \varepsilon_z = \varepsilon_T$ and $\varepsilon_x = \varepsilon_L$.

In the absence of a MM and considering air as the surrounding medium in the coupling region between the two waveguides, the coupling coefficient is approximately 0.53/μm in this structure, corresponding to a coupling length of approximately 3 μm for the x-polarized fundamental mode, as shown in Fig. 14(a). This figure also shows that after incorporating a MM into the gap between the two waveguides in the coupling region, the coupling coefficient is enhanced to approximately 0.58/μm at 0.5 eV chemical potential. The normalized power outputs from port 2 (P_2) and port 4 (P_4) as a function of the graphene chemical potential are shown in Fig. 12(b). From the optical properties of the MM as shown in Fig. 2(b), the imaginary part of the refractive index, which is directly proportional to the loss of the material, is almost negligible from 0.5 to 1.4 eV. Beyond this range, the loss increases drastically. Even though the coupling coefficient reduces monotonically for chemical potential higher than 0.4 eV, to avoid high coupling loss, we restrict our operation within the range of chemical potential from 0.5 to 1.4 eV, as shown in Fig. 14 marked between dashed lines. Within this region, a complete switch of output power from port 2 to port 4 cannot be achieved in this configuration. This is mainly because of the small variation of coupling coefficient over the range of chemical potential. As we theoretically predicted from Eq. (9), the coupling coefficient variation for the TE mode is smaller compared to the TM mode, as shown in Fig. 9. The normalized modal fields for even and odd modes at the cross section of the coupling region are shown in Fig. 15 for chemical potential of 0.5 and 1.4 eV. The arrow stream indicates the field polarization of the modes.

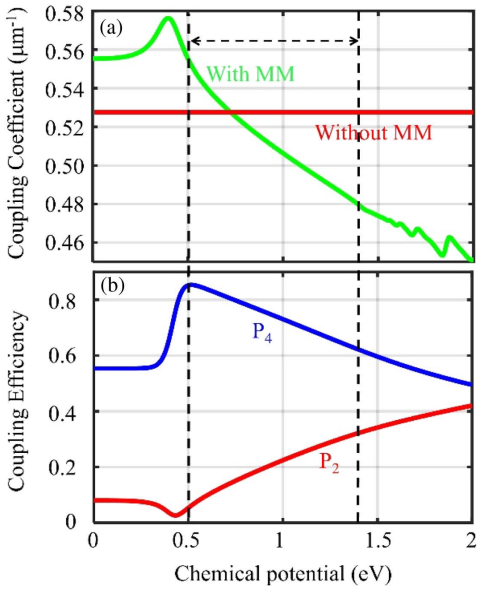

Fig. 14. (a) Coupling coefficient of the coupler with and without MM in the coupling region. (b) Normalized power output from port 2 and port 4 in terms of coupling efficiency as a function of chemical potential.

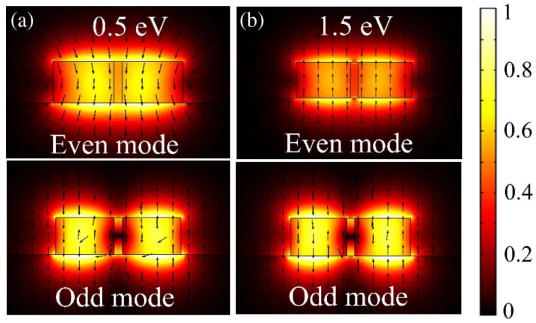

Fig. 15. Normalized electric field plot at chemical potential of (a) 0.5 eV and (b) 1.4 eV.

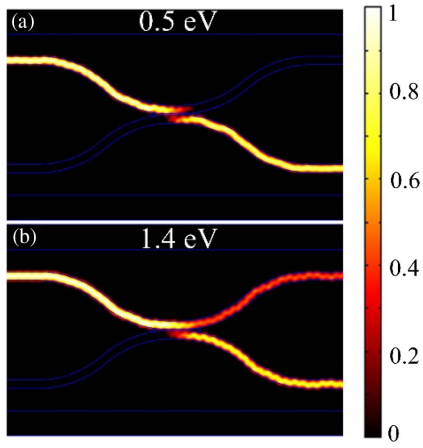

Fig. 16. Normalized electric field plot at chemical potential of (a) 0.4 eV and (b) 1.4 eV.

Normalized electric field profiles of beam propagation through the directional coupler biased at 0.5 and 1.4 eV chemical potential are shown in Figs. 16(a) and 16(b), respectively. At 0.5 eV chemical potential, more than 85% of the power from WG_1 is coupled to WG_2 because of the high coupling coefficient. At 1.4 eV chemical potential, power partitioning into port 2 and port 4 becomes 32% and 62%, respectively.

4. CONCLUSION

We have theoretically investigated the properties of a uniaxial MM composed of periodically stacked monolayer graphene and nanometer-thick HfO_2 in the 1550 nm optical communications wavelength. As the in-plane permittivity of monolayer graphene ($\varepsilon_{GR}^{\parallel}$) can be tuned via externally applied voltage, the anisotropic permittivity of this artificial MM along the transverse direction (ε_T) is also tunable. We have demonstrated a few applications of the proposed MM, such as a polarizer, a modulator, and a tunable directional coupler. Our prototype model of a polarizer shows a tunable extinction ratio between x-polarized and y-polarized EM waves at 1550 nm wavelength by changing the chemical potential of graphene via external application of voltage. Existing graphene-based polarizers [31,32] have much lower extinction ratio without any tunable properties. Depending on its thickness the MM embedded in the middle of the SOI ridge waveguide provides a modulation of the x-polarized guided fundamental mode by switching the chemical potential between 0 and 0.8 eV. Comparing to the existing technology, commercially available and reported devices, such as microring resonator-based modulators [33,34], the device size is at least 3 times greater than our proposed modulator for the same level of performance. Additionally, implementing the proposed anisotropic MM as a dielectric spacer between two waveguides in the coupling region of a directional coupler provides tunable power splitting of a particular guided polarized mode based on the orientation of the MM. The existing technology-based coupler [22,23,35] has a fixed coupling coefficient, which depends on the physical structure of the devices. However, because of the existence of a tunable MM, we have full control on the coupling coefficient, and it can be varied by external application of voltage.

Funding. Air Force Office of Scientific Research (AFOSR) (FA9550-16-1-0152).

Acknowledgment. Alessandro Salandrino acknowledges the support of the Air Force Office of Scientific Research (AFOSR).

REFERENCES

1. A. Alù and N. Engheta, "Light squeezing through arbitrarily shaped plasmonic channels and sharp bends," Phys. Rev. B **78**, 035440 (2008).
2. M. Silveirinha and N. Engheta, "Tunneling of electromagnetic energy through subwavelength channels and bends using ε-near-zero materials," Phys. Rev. Lett. **97**, 157403 (2006).
3. K. Yao and Y. Liu, "Plasmonic metamaterials," Nanotechnol. Rev. **3**, 177–210 (2014).
4. S. Das, R. Halder, and S. K. Varshney, "Triple-core collinear and non-collinear plasmonic photonic crystal fiber couplers," Appl. Opt. **52**, 8199–8204 (2013).
5. C. Haffner, W. Heni, Y. Fedoryshyn, J. Niegemann, A. Melikyan, D. L. Elder, B. Baeuerle, Y. Salamin, A. Josten, U. Koch, and C. Hoessbacher, "All-plasmonic Mach-Zehnder modulator enabling optical high-speed communication at the microscale," Nat. Photonics **9**, 525–528 (2015).
6. T. Wu, Y. Liu, Z. Yu, Y. Peng, C. Shu, and H. Ye, "The sensing characteristics of plasmonic waveguide with a ring resonator," Opt. Express **22**, 7669–7677 (2014).
7. S. Das, A. Salandrino, J. Z. Wu, and R. Hui, "Near-infrared electro-optic modulator based on plasmonic graphene," Opt. Lett. **40**, 1516–1519 (2015).
8. L. Chen, T. Zhang, X. Yin, and X. Li, "Ultra-compact polarization beam splitter utilizing a graphene-based asymmetrical directional coupler," Opt. Lett. **41**, 356–359 (2016).
9. R. Filter, M. Farhat, M. Steglich, R. Alaee, C. Rockstuhl, and F. Lederer, "Tunable graphene antennas for selective enhancement of THz-emission," Opt. Express **21**, 3737–3745 (2013).
10. V. J. Sorger, N. D. Lanzillotti-Kimura, R.-M. Ma, and X. Zhang, "Ultra-compact silicon nanophotonic modulator with broadband response," Nanophotonics **1**, 17–22 (2012).
11. S. Das, S. Fardad, I. Kim, J. Rho, R. Hui, and A. Salandrino, "Nanophotonic modal dichroism: mode-multiplexed modulators," Opt. Lett. **41**, 4394–4397 (2016).
12. S. A. Ramakrishna, J. B. Pendry, M. C. K. Wiltshire, and W. J. Stewart, "Imaging the near field," J. Mod. Opt. **50**, 1419–1430 (2003).
13. S. Feng and J. Elson, "Diffraction-suppressed high-resolution imaging through metallodielectric nanofilms," Opt. Express **14**, 216–221 (2006).
14. D. Schurig and D. R. Smith, "Sub-diffraction imaging with compensating bilayers," New J. Phys. **7**, 162 (2005).
15. P. A. Belov and Y. Hao, "Subwavelength imaging at optical frequencies using a transmission device formed by a periodic layered metal-dielectric structure operating in the canalization regime," Phys. Rev. B **73**, 113110 (2006).
16. P. Alitalo and S. Tretyakov, "Electromagnetic cloaking with metamaterials," Mater. Today **12**(3), 22–29 (2009).
17. A. Salandrino and N. Engheta, "Far-field subdiffraction optical microscopy using metamaterial crystals: theory and simulations," Phys. Rev. B **74**, 075103 (2006).
18. F. Xu, S. Das, Y. Gong, Q. Liu, H. C. Chien, H. Y. Chiu, J. Wu, and R. Hui, "Complex refractive index tunability of graphene at 1550 nm wavelength," Appl. Phys. Lett. **106**, 031109 (2015).
19. L. Yang, T. Hu, A. Shen, C. Pei, B. Yang, T. Dai, H. Yu, Y. Li, X. Jiang, and J. Yang, "Ultracompact optical modulator based on graphene-silica metamaterial," Opt. Lett. **39**, 1909–1912 (2014).
20. Y.-Y. Ji, F. Fan, X.-H. Wang, and S.-J. Chang, "Broadband controllable terahertz quarter-wave plate based on graphene gratings with liquid crystals," Opt. Express **26**, 12852–12862 (2018).
21. M. Chen, F. Fan, L. Yang, X. Wang, and S. J. Chang, "Tunable terahertz amplifier based on slow light edge mode in graphene plasmonic crystal," IEEE J. Quantum Electron. **53**, 8500106 (2017).
22. G. F. R. Chen, J. R. Ong, T. Y. L. Ang, S. T. Lim, C. E. Png, and D. T. Tan, "Broadband silicon-on-insulator directional couplers using a combination of straight and curved waveguide sections," Sci. Rep. **7**, 7246 (2017).
23. Z. Lu, H. Yun, Y. Wang, Z. Chen, F. Zhang, N. A. F. Jaeger, and L. Chrostowski, "Broadband silicon photonic directional coupler using asymmetric-waveguide based phase control," Opt. Express **23**, 3795–3808 (2015).
24. D. L. Wood, K. Nassau, T. Y. Kometani, and D. L. Nash, "Optical properties of cubic hafnia stabilized with yttria," Appl. Opt. **29**, 604–607 (1990)
25. C. Sire, S. Blonkowski, M. J. Gordon, and T. Baron, "Statistics of electrical breakdown field in HfO_2 and SiO_2 films from millimeter to nanometer length scales," Appl. Phys. Lett. **91**, 242905 (2007).
26. Z. H. Zhu, C. C. Guo, K. Liu, J. F. Zhang, W. M. Ye, X. D. Yuan, and S. Q. Qin, "Electrically controlling the polarizing direction of a graphene polarizer," J. Appl. Phys. **116**, 104304 (2014).
27. M. Liu, X. Yin, E. Ulin-Avila, B. Geng, T. Zentgraf, L. Ju, F. Wang, and X. Zhang, "A graphene-based broadband optical modulator," Nature **474**, 64–67 (2011).
28. M. Liu, X. Yin, and X. Zhang, "Double-layer graphene optical modulator," Nano Lett. **12**, 1482–1485 (2012).

29. K. Okamoto, *Fundamental of Optical Waveguides*, 2nd ed. (Academic, 2006).
30. M. Kuznetsov, "Expressions for the coupling coefficient of a rectangular waveguide directional coupler," Opt. Lett. **8**, 499–501 (1983).
31. Q. Bao, H. Zhang, B. Wang, Z. Ni, C. H. Y. X. Lim, Y. Wang, and K. P. Loh, "Broadband graphene polarizer," Nat. Photonics **5**, 411–415 (2011).
32. X. He and J. Liu, "Flexible and broadband graphene polarizer based on surface silicon-core microfiber," Opt. Mater. Express **7**, 1398–1405 (2017).
33. Q. Xu, B. Schmidt, S. Pradhan, and M. Lipson, "Micrometre-scale silicon electro-optic modulator," Nature **435**, 325–327 (2005).
34. J. Hong, F. Qiu, X. Cheng, A. M. Spring, and S. Yokoyama, "A high-speed electro-optic triple-microring resonator modulator," Sci. Rep. **7**, 4682 (2017).
35. Y. Luo, Y. Yu, M. Ye, C. Sun, and X. Zhang, "Integrated dual-mode 3 dB power coupler based on tapered directional coupler," Sci. Rep. **6**, 23516 (2016).